Relaxation properties in a diffusive model of extended objects on a triangular lattice

J.R. Šćepanović [a], Lj. Budinski-Petković [b], I. Lončarević [b], M. Petković [c], Z.M. Jakšić [a], S.B. Vrhovac [a],*

[a] Institute of Physics Belgrade, University of Belgrade, Pregrevica 118, Zemun 11080, Belgrade, Serbia
[b] Faculty of Engineering, Trg D. Obradovića 6, Novi Sad 21000, Serbia
[c] RTRK, Novi Sad 21000, Serbia

ARTICLE INFO

ABSTRACT

In a preceding paper, Šćepanović et al. [J.R. Šćepanović, I. Lončarević, Lj. Budinski-Petković, Z.M. Jakšić, S.B. Vrhovac, Phys. Rev. E 84 (2011) 031109. http://dx.doi.org/10.1103/Phys RevE.84.031109] studied the diffusive motion of k-mers on the planar triangular lattice. Among other features of this system, we observed that the suppression of rotational motion results in a subdiffusive dynamics on intermediate length and time scales. We also confirmed that systems of this kind generally exhibit heterogeneous dynamics. Here we extend this analysis to objects of various shapes that can be made by self-avoiding random walks on a triangular lattice. We start by studying the percolation properties of random sequential adsorption of extended objects on a triangular lattice. We find that for various objects of the same length, the threshold ρ_p^* of more compact shapes exceeds the ρ_p^* of elongated ones. At the lower densities of ρ_p^*, the long-time decay of the self-intermediate scattering function (SISF) is characterized by the Kohlrausch–Williams–Watts law. It is found that near the percolation threshold ρ_p^*, the decay of SISF to zero occurs via the power-law for sufficiently low wave-vectors. Our results establish that power-law divergence of the relaxation time τ as a function of density ρ occurs at a shape-dependent critical density ρ_c above the percolation threshold ρ_p^*. In the case of k-mers, the critical density ρ_c cannot be distinguished from the closest packing limit $\rho_{CPL} \lesssim 1$. For other objects, the critical density ρ_c is usually below the jamming limit ρ_{jam}.

© 2012 Elsevier B.V. All rights reserved.

1. Introduction

In the past two decades, a large number of observations related to anomalous diffusion [1] have been reported in several fields of physics and related sciences. Recent attention focuses on the anomalous slow dynamics in a broad variety of systems such as colloidal gels [2], porous materials [3–6], glass forming systems [7,8], granular fluids [9,10] and biological media [11,12]. The signature of subdiffusion is that the mean square displacement of particles grows sublinearly with time, which may be related to the non-Markovian nature of the stochastic process present in these systems. The reduced mobility is often accompanied by dynamical heterogeneities [13,14] and cooperative motion [15]. A system is considered as dynamically heterogeneous if dynamically distinguishable populations of particles with different mobilities can be isolated by a computer simulation or experiment. Deviations of the van Hove correlation function from the Gaussian behavior are usually ascribed to the presence of particles that are substantially faster or slower than the average [13,14].

---

* Corresponding author.
  E-mail address: vrhovac@ipb.ac.rs (S.B. Vrhovac).
  URL: http://www.ipb.ac.rs/~vrhovac/ (S.B. Vrhovac).

In a preceding paper [16], we studied a model of the diffusive motion of k-mers on the planar triangular lattice. In this model, the moves of a randomly chosen k-mer can be either translation along its axis or rotation when k-mer changes its orientation. The only interactions between the particles are the geometrical ones, i.e., we allow only the single-k-mer moves that do not cause double occupation at any site. In the absence of rotation, a k-mer can only move along one of the three axis bisecting the triangular lattice. In this case, the model can serve as an example of mutually intersecting arrays of single-file systems ("channels") [17]. Prominent examples of such systems are zeolites of MFI structure type like ZSM-5 [18,19].

The analysis in Ref. [16] pertained mainly to relaxation process at densities high enough that the mean-squared displacements exhibit a subdiffusive behavior at intermediate times between the initial transient and the long-time diffusive regime. We have shown that there is a pronounced deviation of the van Hove correlation function from the Gaussian distribution, especially at high densities. We have found that the decay of self-intermediate scattering function (Eq. (6)) to zero occurs via the Kohlrausch–Williams–Watts law (Eq. (7)) for all values of the wave vector q_n and for all densities investigated. We have shown that for dimers, relaxation times display a power-law divergence at densities around the closest packing limit $\rho_{CPL} \lesssim 1$. The time scale and the diffusion coefficient show qualitatively the expected behavior as a function of density, since the inverse of the self diffusion coefficient D_s also seems to diverge with the power law at the maximum density ρ_{CPL}. These studies have shown that our model reproduces many aspects of the dynamics of glass-forming systems, e.g., the slowing-down of the dynamics on increasing the density suggesting the existence of a transition of structural arrest at ρ_{CPL}.

The purpose of this paper is to extend the analysis in Ref. [16] to objects of various shapes that can be made by self-avoiding random walks on a triangular lattice [20]. We address the following questions: (1) How does particle shape modify slow dynamics in our diffusive lattice model? (2) How do various objects promote or suppress kinetic arrest of the system depending on degree of shape anisotropy? Our approach can provide some answers to such questions because the slowing-down of the dynamics in the model can be understood as a consequence of steric effects, that make certain moves of particles impossible owing to an effective high local density.

Now, we sketch the main features of our model. The system is initialized by the random sequential adsorption (RSA) model [21–24]. In two dimension (2D), RSA is a process in which the objects of a specified shape are randomly and sequentially deposited onto a substrate. Excluded volume, or particle–particle interaction, is incorporated by rejection of deposition overlap, while the particle–substrate interaction is modeled by the irreversibility of deposition. The deposition process ceases when all unoccupied spaces are smaller than the size of an adsorbed particle. The system is then jammed in a nonequilibrium disordered state for which the limiting (jamming) coverage ρ_{jam} is less than the corresponding density of closest packing ρ_{CPL}. However, when adsorbed particles are allowed to diffuse, jammed configurations can be relaxed by particle movement (RSAD models). Jamming density in RSAD models is higher and in some cases closest packing density is reached [24]. Random closest packing states are characterized by the absence of mobile particles. At a predetermined density $\rho_0 < \rho_{CPL}$, the deposition is terminated and random diffusive dynamics is initiated in our system. In general, objects have both translational and rotational motion. However as we focus on the subdiffusive behavior, we suppress the rotational motion of objects.

As a first step toward answering the above questions, we analyze the percolation properties of random sequential adsorption of extended objects on a triangular lattice. Dynamical behavior of model at large length scales is studied via the mean square displacement of a particle (MSD, Eq. (3)). We evaluate the relaxation times by studying the time decay of the self-part of the intermediate scattering function (SISF, Eq. (6)). In particular, we analyze the relaxation time dependence both on the wave-vector (length scale) and on the density of the system. Most of our attention is focused on the influence of shape on the temporal behavior of MSD and SISF.

In Section 2 we introduce our model and give some details of our simulations. We present the simulation results and discussions in Section 3. Finally, Section 4 contains some additional comments and final remarks.
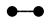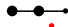
2. Definition of the model and the simulation method

We study the random diffusion of extended objects on a planar triangular lattice with fixed density, where the interparticle interaction is limited to hard-core exclusion up to the nearest neighbors. The initial state of the system is prepared through the random sequential adsorption (RSA) model where by deposition of particles we reach the desired value of the density. The depositing objects are made by directed self-avoiding random walks on the lattice. On a triangular lattice objects with a symmetry axis of first, second, third and sixth order can be formed. Rotational symmetry of order n_s, also called n_s-fold rotational symmetry, with respect to a particular axis perpendicular to the triangular lattice, means that rotation by an angle of $2\pi/n_s$ does not change the object. We performed numerical simulations for all such shapes of length $\ell = 1$, 2 and 3, covering two, three and four lattice sites, respectively. All these objects are shown in Table 1. On a triangular lattice it would also be interesting to examine the behavior of a hexagon shown in Table 1.

We start with an initially empty triangular lattice. At each Monte Carlo step a lattice site is selected at random. If the selected site is unoccupied, deposition of the object is tried in one of the six orientations. We fix both the direction and the beginning of the walk that makes the shape at the selected site and search whether all successive ℓ sites are unoccupied. If so, we occupy these $\ell + 1$ sites and place the object. If the attempt fails, a new site and a new direction are selected at random. The coverage of the surface is increased by inserting the objects randomly up to the chosen coverage fraction ρ_0. In this way we are able to prepare the system in disordered initial state with a statistically reproducible density ρ_0.

Table 1

Jamming coverage $\rho_{jam}^{(x)}$, and the percolation threshold $\rho_p^{(x)}$ for various basic shapes (x) of length $\ell^{(x)}$ on a triangular lattice. The colors are associated with the different order $n_s^{(x)}$ of symmetry axis. Two adjacent nodes corresponding to the first step in the formation of the objects are indicated by large points.

(x)	Shape	$n_s^{(x)}$	$\ell^{(x)}$	$\rho_{jam}^{(x)}$	$\rho_p^{(x)}$
(A)		2	1	0.9139 (5)	0.4841 (13)
(B)		2		0.8362 (7)	0.4611 (9)
(C)		1	2	0.8345 (8)	0.4585 (11)
(D)		3		0.7970 (4)	0.5214 (9)
(E)		2		0.7886 (8)	0.4399 (12)
(F)		1		0.7653 (10)	0.4304 (12)
(G)		1		0.7739 (7)	0.4815 (11)
(H)		2	3	0.7404 (9)	0.4369 (11)
(I)		1		0.7226 (6)	0.4461 (5)
(J)		2		0.7593 (4)	0.5387 (6)
(K)		6	6	0.6695 (7)	0.5836 (11)

Then, we switch the deposition events off and initiate a random diffusive dynamics in our system. At this stage, apart from the hard core interaction there are no other interactions between the particles. At each Monte Carlo step, we allow only the single-object moves that do not cause a double occupation at any site at any time. For each object that placed on the lattice, we can define its own axis. The axis of an object is a direction that is determined by the direction of the first step in the formation of the object on the grid. For each object, two adjacent nodes corresponding to the first step in its formation are indicated in Table 1. These nodes define the axis of each object deposited on the lattice. There are two kinds of moves that we could allow. First, there may be shifts in which an object simply translates along its own axis, which we call a glide. Furthermore, there may be moves in which an object changes its orientation, which we call a rotation.

In our algorithm, a diffusion event is tried only if there is a beginning of a deposited object at the randomly selected site, otherwise the attempt is rejected. If only glide moves are allowed in the model, we pick one of the two possible directions along the object axis at random, with equal probability, and try to move the selected object by one lattice spacing in that direction. The object is moved if it does not overlap with any of the deposited objects. If the attempted move is not possible, the object stays at its original position.

If both rotations and glides of objects are allowed, a single object can move in any of the six possible directions, so that orientations of particles are not kept fixed. In our model the glide and rotation attempts are statistically independent and they perform sequentially with corresponding probabilities. At each Monte-Carlo step a glide is attempted with probability $P_{gl} = 1$ and rotation with probability $P_{rot} \leq 1$. Rotation process starts by choosing a lattice site at random. If this selected site is unoccupied, the rotation step fails and the process continues by choosing a new site for the glide attempt. On the other hand, if a beginning of a deposited object is at the selected site, one of the six possible orientations is chosen at random and rotation of the object is tried with probability P_{rot} in that direction. The object is rotated if it does not overlap with any of the deposited objects. On the contrary, the attempt is rejected.

The Monte-Carlo simulations are performed on the triangular lattice of size $L \times L = 60^2$ with periodic boundary conditions. For convenience we have assumed that the lattice spacing is one. The time is counted by the number of glide attempts and scaled by the total number of lattice sites. The data are averaged over 20 independent runs for each of the investigated densities.

3. Results and discussion

In this section we present and discuss the results of our simulations. The first subsection deals with percolation properties of the model. In the next subsections we analyze the mean-square displacement of the particles and density–density autocorrelation functions.

3.1. Percolation transition

It would be interesting to compare the results describing dynamic properties of our diffusive model with the percolation properties of non-overlapping objects on the lattice. In order to obtain the values of the percolation thresholds for the

objects of interest, additional simulations were performed on a triangular lattices of various sizes ranging from $L = 50$ to $L = 1000$. Hard boundary conditions are used in the horizontal direction, in which the onset of percolation is detected. The periodic boundary conditions are applied in the other directions. The data are averaged over 100 independent runs for each depositing object. The coverage of the surface is increased in the deposition process up to the percolation threshold, when there appears a cluster that extends through the whole system. We say that a percolating cluster arises in the system when the opposite edges of the system are connected via some path of nearest neighbor sites occupied by the particles. Here we check the connectivity between left and right edges of the lattice. The tree-based union/find algorithm implemented on a grid platform was used to determine the percolation threshold [25]. Another quantity of interest is the jamming limit ρ_{jam} which is reached when no more depositing objects can be placed in any position on the lattice. Details of these simulations are given elsewhere [26,27].

According to the standard finite-size scaling theory of percolations [28], it is expected that:

(a) the effective percolation threshold ρ_p (the mean value measured for a finite lattice) approaches the asymptotic value ρ_p^* ($L \to \infty$) via power law

$$\rho_p - \rho_p^* \propto L^{-1/\nu}, \tag{1}$$

where ν is then critical exponent. This relationship allows us to extrapolate the threshold for an infinite system, $L \to \infty$.

(b) the standard deviation σ of the percolation threshold measured for a finite lattice L satisfies the power law

$$\sigma \propto L^{-1/\nu}. \tag{2}$$

Fig. 1 shows the finite-size scaling of L-dependent quantities ρ_p and σ. We have used the value of the correlation length exponent ν corresponding to the two-dimensional percolation universality class [28], that is $\nu = 4/3$.

Finite-size scaling of the effective percolation threshold ρ_p against $L^{-1/\nu}$ is illustrated in Fig. 1(a) for dimers (A), angled objects (C), triangles (D) and for objects (F), (G), (H), (I), (J) and (K) from Table 1. Values of the obtained percolation thresholds ρ_p^* for various objects are given in Table 1 together with the corresponding jamming coverages ρ_{jam}. Plotting the standard deviation σ vs. L (Fig. 1(b)) on a double logarithmic scale for dimer (A), angled object (C), triangle (D), and hexagon (K), the validity of the finite-size scaling (2) in the system was confirmed. We observe that the symmetry order n_s of the shape is not correlated with the percolation threshold for various objects. But, our results suggest that for various objects of the same length ℓ, the percolation threshold ρ_p^* of more compact shapes exceeds the ρ_p^* of the elongated ones. Indeed, if $\ell = 3$ then the largest thresholds are observed for the objects (J) and (G). Object (J), with the largest threshold, has the smallest number m of the first neighboring sites on the lattice, i.e. $m = 10$. For the second object (G), we have $m = 11$, while for all other objects of the length $\ell = 3$, $m = 12$. Consequently, objects (I), (E), (H), and (F) have significantly lower thresholds. Hence, the percolation threshold decreases with m for the objects of the same length. Qualitatively, we could say that object capability to make connections with other depositing objects depends on the number m of the first neighboring sites on the lattice.

3.2. Diffusion properties

In the following, we analyze the mean square displacement (MSD) of a particle, $\langle \Delta r^2(t) \rangle$, defined as

$$\langle \Delta r^2(t) \rangle = \frac{1}{N} \left\langle \sum_{i=1}^{N} |\vec{r}_i(t) - \vec{r}_i(0)|^2 \right\rangle, \tag{3}$$

where $\vec{r}_i(t)$ is the two-dimensional trajectory of particle i, and N is the number of deposited objects of length ℓ, i.e. $N = \rho_0 L^2/(\ell + 1)$. The angular brackets $\langle \cdot \rangle$ here and in the following denote an average over the simulation ensemble in which the coverage fraction ρ_0 of the system is fixed. Anomalous diffusion is characterized through the power law form

$$\langle \Delta r^2(t) \rangle = K_\alpha t^\alpha \tag{4}$$

of the MSD deviating from the well-known property $\langle \Delta r^2(t) \rangle \propto t$ of Brownian (normal) diffusion. According to the value of the anomalous diffusion index α, one distinguishes subdiffusion ($0 < \alpha < 1$) and superdiffusion ($1 < \alpha \leq 2$) [29,1]. In the case of normal diffusion, the self-diffusion coefficient is given by the slope of the MSD at large times according to

$$D_s = \lim_{t \to \infty} \frac{\langle \Delta r^2(t) \rangle}{4t}. \tag{5}$$

We now turn our attention to analysis of the diffusive motion of various objects from Table 1 in the case when only glide moves are allowed (i.e., $P_{rot} = 0$). The MSD for 3-mers (B) and angled objects (C) are shown in Fig. 2(a) and (b), respectively, for a wide range of packing fractions $0.10 \leq \rho_0 \leq 0.83$. The curves have been plotted in a log–log scale in order to display the flattening-out behavior of the MSD at intermediate times. At short times objects do not feel the presence of their neighbors and they move freely. At very low densities (not shown here), the initial transient is followed by the usual diffusive linear
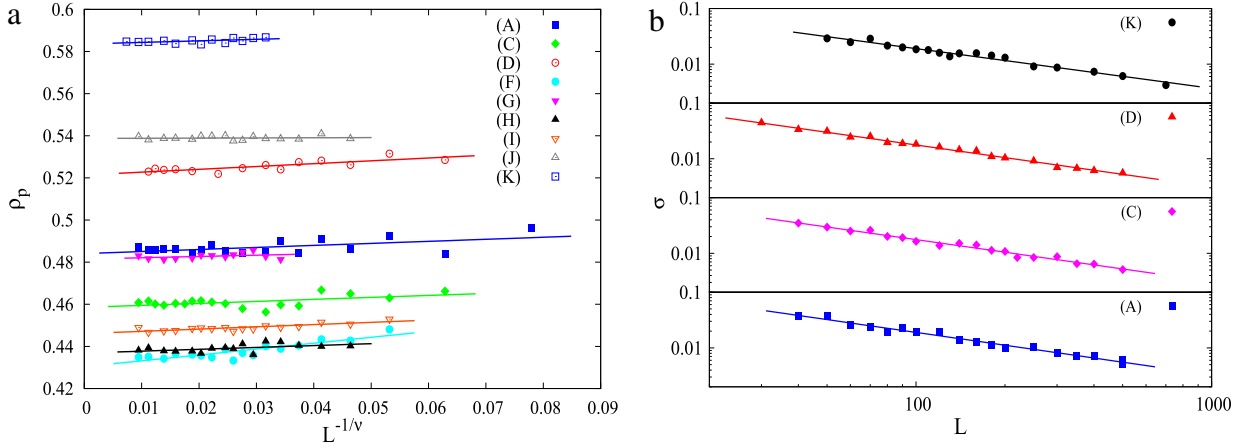
Fig. 1. (Color online) (a) Finite-size scaling of the percolation threshold ρ_p against $L^{-1/\nu}$ with $\nu = 4/3$ for objects (A), (C), (D), (F), (G), (H), (I), (J), and (K) from Table 1. (b) Standard deviations σ of the percolation threshold on double logarithmic scale for dimer (A), angled object (C), triangle (D), and hexagon (K). Straight lines correspond to the best fit according to the power law of Eq. (2) and with the exponents 0.765 ± 0.015, 0.754 ± 0.017, 0.755 ± 0.017 and 0.714 ± 0.018 for objects (A), (C), (D) and (K), respectively. Apart from slight deviations for the hexagon (K), these results are in good agreement with the universal value $1/\nu = 3/4$.
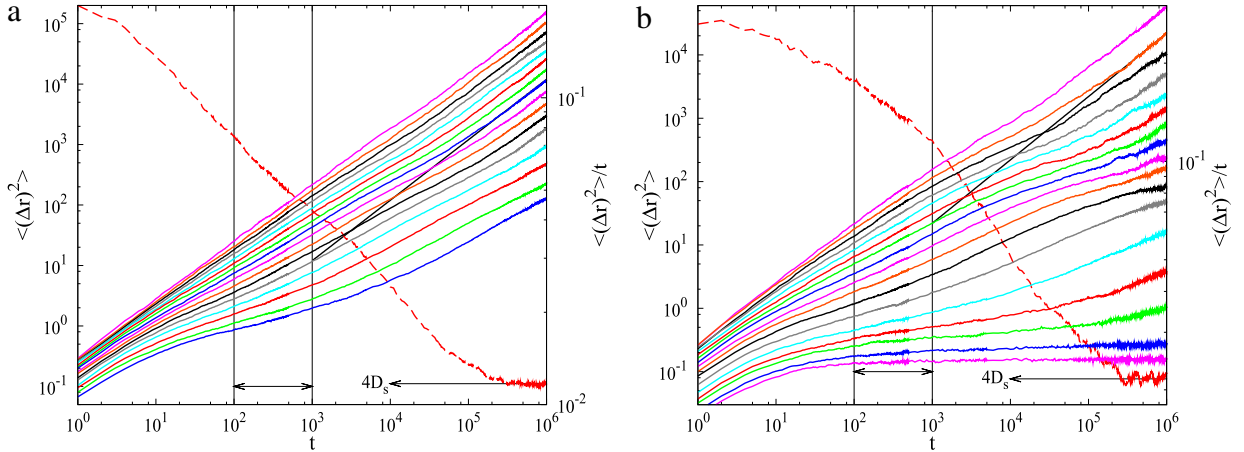

Fig. 2. (Color online) Shown here are the double logarithmic plots of the temporal evolution of the MSD for (a) 3-mers (B), and (b) angled objects (C) at various densities ρ_0. The solid lines represent the MSD versus time t for densities (a) $\rho_0 = 0.10 + 0.05n$ ($n = 0, 1, 2, \ldots, 14$), 0.83, and (b) $\rho_0 = 0.10 + 0.05n$ ($n = 0, 1, 2, \ldots, 12$), 0.73, 0.75, 0.78, 0.80, from top to bottom (left-hand axis). The dashed lines are plotted against the right-hand axis and give the temporal evolution of the MSD divided by t, for densities (a) $\rho_0 = 0.45$, and (b) $\rho_0 = 0.15$. The horizontal arrows at (a) $4D_s = 0.0117$, and (b) $4D_s = 0.0216$ represent the average value of $\langle \Delta r^2(t) \rangle / t$, for large t. Additionally, the slanted straight lines with the unit slope are shown, indicating the late time diffusive behavior, $\langle \Delta r^2(t) \rangle = 4D_s t$, in the case of (a) $\rho_0 = 0.45$, and (b) $\rho_0 = 0.15$. For the time region between the thin vertical lines, it is possible to fit the MSD data with a power law (4).

dependence on t. However, for high densities an intermediate region develops where the system is subdiffusive. As an illustration, the two dashed lines representing the temporal evolution of the MSD divided by t, $\langle \Delta r^2(t) \rangle / t$, are included in Fig. 2. In that case, normal diffusion yields a line of slope 0, and subdiffusion yields a line of negative slope. As seen from Fig. 2, region of anomalous diffusion can extends over several decades of time, before eventually entering the diffusing regime. The larger the density ρ_0 is, the larger the subdiffusion regime is. For angled objects (C) and densities $\rho_0 \gtrsim 0.25$ a sublinear time dependence of MSD extends until the limit of our simulations ($t = 10^6$).

Values of the fitting parameter α are determined from the slopes of $\langle \Delta r^2(t) \rangle$ versus t curves in certain time regions. In the range $t \in [10^2, 10^3]$ (time region between the thin vertical lines in Fig. 2), the exponent α is less than 1 for all the densities considered and decreases with density ρ_0. In particular, values of parameter α for objects (B) and (C) do not exceed, respectively, 0.90 and 0.86, which are the values found for the lowest density, i.e., $\rho_0 = 0.10$. As expected, in the limiting case of high densities, the value of exponent α tends to 0; the subdiffusion at intermediate times becomes stronger with increasing density and finally the system is frozen in a particular configuration on the time scale of our simulations. However, there is a significant difference in the behavior of the 3-mers (B) and angled objects (C). In the case of the object (B), the critical density ρ_c at which significant structural changes occur in the system is approximately equal

to the closest packing limit, $\rho_{CPL} \lesssim 1$, for 3-mers on the two-dimensional triangular lattice [30–32]. This would suggest that there is no critical density lower than the closest packing limit at which a structural arrest of the system occurs. However, the critical density $\rho_c \approx 0.80$ for which there is no more diffusion of particles (C) is much smaller than the jamming density $\rho_{jam} = 0.8362$. This would suggest that there is a dynamical transition in this case. We shall return to this point later on in connection with the relaxation times by studying the time decay of the self-part of the intermediate scattering function.

Upon analyzing trajectories of particles in the course of a simulation run these findings can be interpreted as follows. On short time scales, the rise of $\langle \Delta r^2(t) \rangle$ is due to the diffusion of particles before they start feeling the presence of their neighbors. Beyond this time scale, particles are temporarily trapped in cages formed by their neighbors and as a consequence, the collisions within the cage result in a time dependence of the MSD that is slower than the unity, $\alpha < 1$. At long times, the motion of particles is not restricted by a shell of nearest neighbors, and their movement is then less and less influenced by the effect of trapping, so that the exponent α in Eq. (4) increases ($\alpha \rightarrow 1$). This corresponds to the well-known cage effect observed in supercooled liquids [33–35], dense colloidal systems [36,7], and granular fluids [9,37,38]. For sufficiently high densities ρ_0, the trapping configurations are frozen and then we observe only "cage rattling motion" of particles during the simulation run.

In Fig. 3 we compare the temporal evolution of the MSD at density $\rho_0 = 0.65$ for various objects from Table 1. As can be seen, the MSD of 3-mers (B) significantly exceeds the MSD of the other objects at intermediate and large times. This is a consequence of the fact that the dynamics of an object moving on a lattice is dictated by the geometric exclusion effects. Let us explain this fact on the example of gliding movement of objects (B) and (F). Both objects cover three nodes along its axis. These objects diffuse along straight lines ("channels"), where the mutual particle exchange between the channels is excluded. The single filing constraint is relaxed in such system, because some lattice points in the channel along one specific direction can be occupied by particles moving along the other directions. For the angled object (F) diffusing in mutually intersecting channel arrays less possible places for displacement are allowed than for the linear segment (B). Accordingly, from Fig. 3 it is evident that particle diffusivity may be reduced if the object covers nodes outside its own axis. The critical density ρ_c for some shapes with such constitutive property is mostly below jamming density. For example, the values of ρ_c for objects (C), (D), (F), and (I) are $\rho_c \lesssim 0.80$, 0.86, 0.75, and 0.66, respectively. It is important to note that the subdiffusion at intermediate times becomes stronger with increasing the objects size for the same density [16].

We analyze in the following the MSD of particles in the case of simulations where both rotations ($P_{rot} > 0$) and glides of objects are allowed simultaneously. In Fig. 4 we compare the temporal evolution of the MSD for angled objects (C) at density $\rho_0 = 0.80$ for various rotation probabilities $P_{rot} = 10^{-4} - 1.0$. Note that in the absence of rotation (Fig. 2(b)), such a high density system does not evolve any more on the time scale of our simulations. At high values of $P_{rot} \lesssim 1$, short initial transient goes over immediately into a diffusive behavior. For low rotation probabilities, a plateau develops, indicating that a cage has formed, which restricts the particles motion to the space within the cage. Accordingly, the system becomes subdiffusive over an intermediate time window that becomes broader as P_{rot} decreases. The long-time particle diffusivity D_s (inset of Fig. 4) appears to increase with P_{rot}. Furthermore, for the fixed value of P_{rot}, the self-diffusion coefficient D_s decreases algebraically with the density ρ_0, which is consistent with results previously obtained in similar models [39–41].

3.3. Relaxation dynamics

In order to investigate the relaxation dynamics over different length scales we study the self intermediate scattering function $F_s(\vec{q}, t)$ (SISF) given by

$$F_s(\vec{q}, t) = \frac{1}{N} \left\langle \sum_{i=1}^{N} \exp\{i\vec{q} \cdot [\vec{r}_i(t) - \vec{r}_i(0)]\} \right\rangle, \tag{6}$$

where, again, $\vec{r}_i(t)$ is the position of the i-th particle in units of the lattice constant. Due to periodic boundary conditions, the wave vector $\vec{q}$ can take the discrete values $\vec{q} = (2\pi/L)\vec{n}$, where $\vec{n} = (n_x, n_y)$ has integer components n_x and n_y ranging from 0 to $L/2 = 30$. In dense colloids and supercooled liquids, $F_s(q_n, t)$ displays a multi-step decay. At short times relaxation is coming from free and collisional events that involve local particle motion. Intermediate times include a period during which particles appear trapped in cages formed by other particles. This regime is the β-relaxation regime. At long times, in the α-relaxation regime, the decay corresponds to particle diffusion out of the cage. The time scale of the α relaxation diverges as the glass transition approached.

First, we investigate the relaxation dynamics of extended objects when the rotation moves can never occur, i.e. $P_{rot} = 0$. Fig. 5 presents our results for the self-intermediate scattering function $F_s(q_n, t)$ of objects (C) and (I) at density $\rho_0 = 0.45$, for various wave vectors. We choose $\vec{q} = (q_n, 0)$, where $q_n = (2\pi/L)n$ and $n = 1, 2, 4, 6, 8, 10, 16, 20, 24, 30$. As can be seen, $F_s(q_n, t)$ decays more slowly the smaller q_n is. Contrary to the usual behavior observed in supercooled liquids and predicted by the mode-coupling theory, we do not observe a plateau in the decrease of $F_s(q_n, t)$. Our results show that $F_s(q_n, t)$ curves stay close to unity for a time span that increases with increasing density. Similar behavior has also been observed in the Kob–Andersen kinetic lattice gas model, kinetically constrained spin models and in sheared granular materials close to the
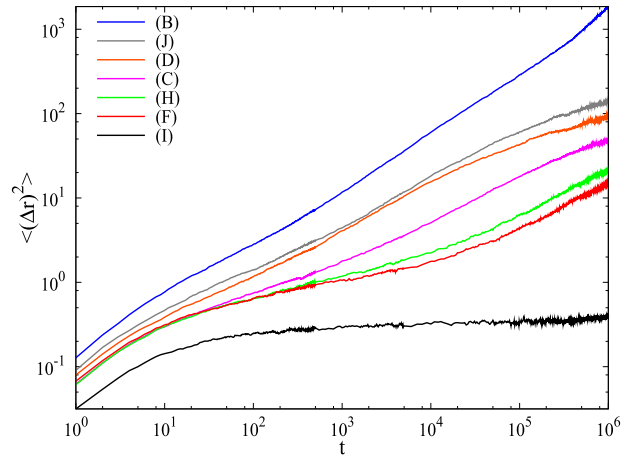
Fig. 3. (Color online) Shown here is the double logarithmic plot of the temporal evolution of the MSD for various objects from Table 1, as indicated in the legend, at density $\rho_0 = 0.65$.
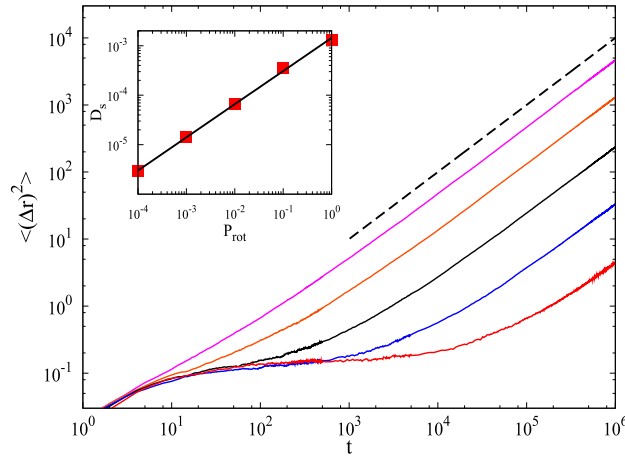

Fig. 4. (Color online) Shown here is the double logarithmic plot of the temporal evolution of the MSD for angled objects (C) in the case of $\rho_0 = 0.80$ and for various rotation probabilities P_{rot}. The solid lines represent the MSD versus time t for probabilities $P_{rot} = 1.0, 0.1, 0.01, 0.001, 0.0001$, from top to bottom. The dashed straight line is shown, indicating the late time diffusive behavior, $\langle \Delta r^2(t) \rangle = 4D_s t$. Inset: the self-diffusion coefficient D_s for dimers as a function of the rotation probability P_{rot}. The solid straight line is the power-law fit, $D_s \propto P_{rot}^{0.67}$.

jamming transition [39,42,43]. In our model, the absence of the rattling motion of caged particles causes that the value of the plateau is unity or very close to it. Thus the early time β regime would be very difficult or impossible to observe.

Density value of $\rho_0 = 0.45$ is close to the percolation thresholds ρ_p (see Table 1) for the objects (C) and (I) on the triangular lattice. Close to the percolation threshold ρ_p, at sufficiently low wave vectors the long time decay starts to follow a power law behavior $F_s(q_n, t) \propto t^{-c}$, as is shown by the double logarithmic plot of Fig. 5. This relaxation pattern suggests that the relaxation over length scales of the order of the system size is controlled by the onset of the percolating cluster [44].

In Fig. 6, we show $F_s(q_n, t)$ of objects (C) and (I) at various densities ρ_0 for one particular wave vector $q_n = 2\pi/15$ ($n = 4$). For the case of high densities, due to the very slow dynamical relaxation, only a part of the $F_s(q_n, t)$ can be observed at small values of the wave vector q_n. Analyzing the curves in Fig. 6 we find that the decrease of $F_s(q_n, t)$ is slower than exponential in time. As density ρ_0 is increased toward the percolation threshold, $F_s(q_n, t)$ displays a long time decay well fitted by a stretched exponential law

$$F_s(q_n, t) = A \exp\left[-\left(\frac{t}{\tau(q_n)} \right)^{\alpha(q_n)} \right], \tag{7}$$

where $\alpha(q_n)$ is the parameter measuring the deviation from the single exponential form ($0 < \alpha \leq 1$) and $\tau(q_n)$ is the relaxation time. Fits of this stretched exponential form to the simulation data are shown as dot-dashed lines in Fig. 6. This long time behavior can be related to the cluster size distribution close to the percolation threshold, which produces relaxation processes taking place over different length scales. Near the percolation threshold, the onset of a power law decay is observed at low wave vectors, indicating that the relaxation over sufficiently large length scale is controlled by
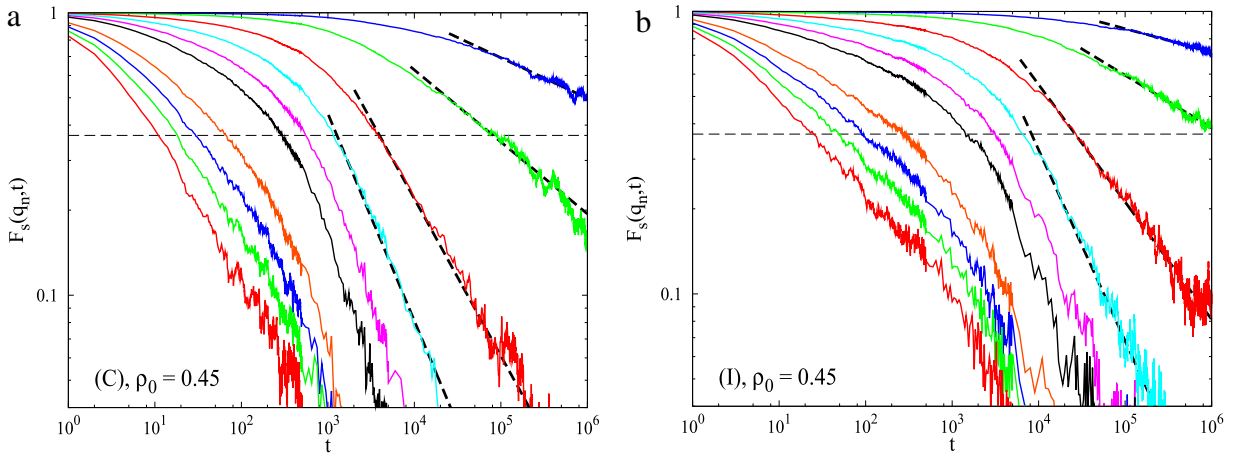
Fig. 5. (Color online) The time dependence of the $F_s(q_n, t)$ for objects (C) and (I) at density $\rho_0 = 0.45$. The curves in graphs (a) and (b) correspond to the wave vectors $\vec{q} = (q_n, 0)$, where $q_n = (2\pi/L)n$ and $n = 30, 24, 20, 16, 10, 8, 6, 4, 2, 1$ (from left to right). At $n = 1, 2, 4, 6$ the data are fitted by a power law $\propto t^{-c}$ (straight dashed lines). The horizontal dashed line indicates the $1/e$ value.
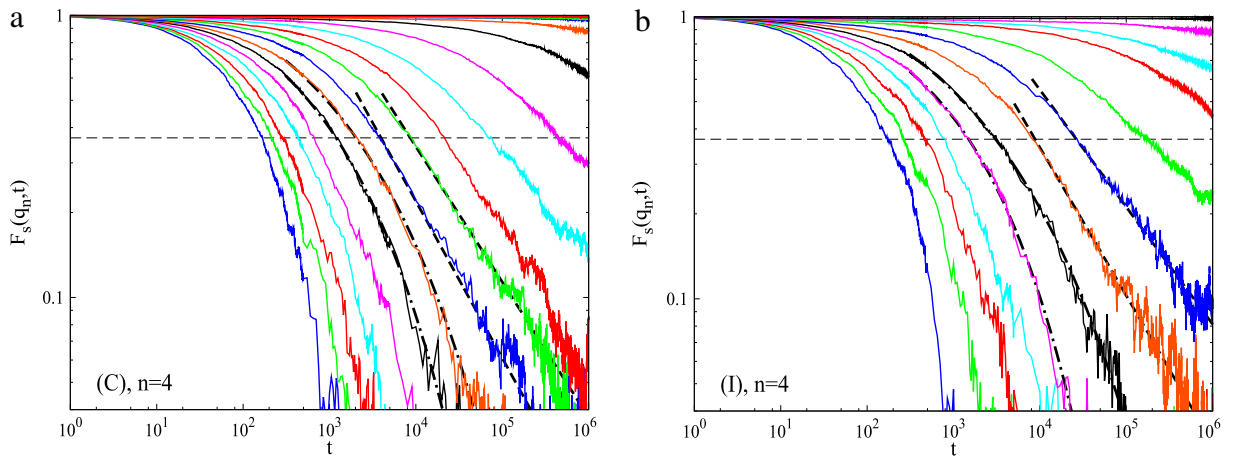

Fig. 6. (Color online) The time dependence of the $F_s(q_n, t)$ for objects (C) and (I) for various densities. The curves in graphs correspond to the wave vector $q_n = 2\pi/15$ ($n = 4$) and densities (from left to right): (a) $\rho_0 = 0.10 + 0.05n$ ($n = 0, 1, 2, \ldots, 12$), 0.73, 0.75, 0.76, 0.78 and (b) $\rho_0 = 0.10 + 0.05n$ ($n = 0, 1, 2, \ldots, 9$), 0.57, 0.60, 0.65. The dot-dashed curves are the stretched exponential fits of Eq. (7). At densities close to the percolation threshold the data are fitted by a power law $\propto t^{-c}$ (straight dashed lines). The horizontal dashed line indicates the $1/e$ value.

the formation of percolating cluster. It is interesting to notice that these dynamic features agree with results obtained by numerical simulations of lattice based gelation models [45–48].

We study now the wave-dependent relaxation time $\tau(q_n)$ that can be obtained from the simulation curves of $F_s(q_n, t)$ as time τ such that $F_s(q_n, \tau) = 1/e$. For the highest densities, the small-q components of SISF do not decay to $1/e$ within the simulation time. In that case, we estimate $\tau(q_n)$ by optimizing the collapse on the master curve. In Fig. 7 we show the parameter $\tau(q_n)$ for objects (B), (C), (D), and (I) as a function of the wave vector, in the case of two densities, $\rho_0 = 0.10$ and 0.50. As expected, for sufficiently low values of density ($\rho_0 \lesssim 0.10$) we obtain that the relaxation time $\tau(q_n)$ scales as q_n^{-2}. Hence, at low densities objects perform a normal diffusive motion on large length and time scales, and therefore $F_s(q_n, t) \propto \exp(-D_s q_n^2 t)$. However, the relation $q_n^2 \tau(q_n) D_s = 1$ ceases to be valid for higher densities $\rho_0 \gtrsim 0.10$. We note that different choices of objects give qualitatively similar results. In Fig. 8 we show the q_n dependence of the relaxation time $\tau(q_n)$ of object (C), for various densities, $\rho_0 = 0.10 - 0.65$. It can be easily seen that, especially for large densities, there is a pronounced deviation of the slopes of τ vs. q_n curves from -2. A slope stronger than -2 when τ is plotted vs. q_n using the log–log axes is the signature of subdiffusion.

In the following we present our results of the analysis of the relaxation time τ as a function of the density ρ_0. In a previous paper [16], we showed that for dimers, the slowing down of the dynamics with ρ_0 is consistent with a scaling law

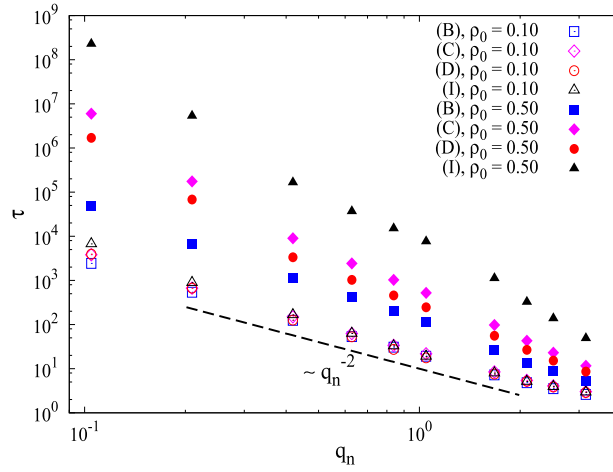$$\frac{1}{\tau(q_n; \rho_0)} = S(q_n)(\rho_c - \rho_0)^{\varkappa}. \tag{8}$$

Fig. 7. (Color online) Shown here is the double logarithmic plot of the relaxation time $\tau(q_n)$ for the objects (B), (C), (D), and (I), as a function of the wave vector q_n. The results correspond to densities $\rho_0 = 0.10$ (empty symbols) and 0.50 (full symbols). The dashed black line has slope -2 and is a guide for the eye.
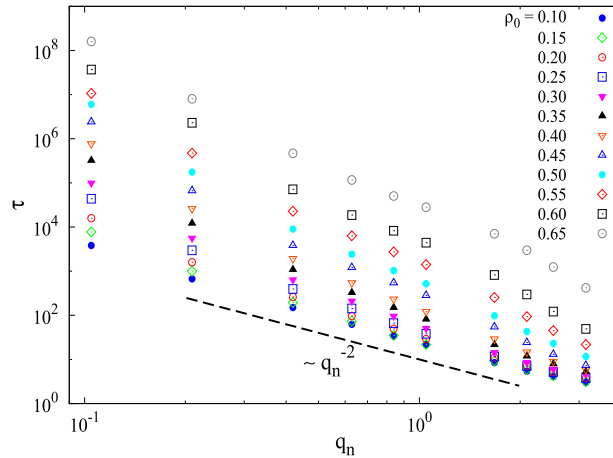

Fig. 8. (Color online) The relaxation time $\tau(q_n)$ for the case of object (C), as a function of the wave vector q_n. The symbols correspond to densities $\rho_0 = 0.10 + 0.05n$, $(n = 0, 1, 2, \ldots, 11)$ as indicated in the legend. The dashed black line has slope -2 and is a guide for the eye.

This functional dependence of relaxation has also been found in many numerical lattice gas models [39,49,50]. In the case of dimers [16], our analysis predicted that the power law divergence (8) for the time scale τ occurs at the density of closest packing of dimers on the 2D triangular lattice, $\rho_c \lesssim 1$ [30–32], and that the exponent $\varkappa$ remains nearly constant ($\varkappa = 3.34 \pm 0.12$) regardless of the value of wave-vector q_n. This would suggest that there is no critical density lower than the closest packing limit at which a structural arrest of the system occurs.

Fig. 9 shows the wave-vector dependent inverse relaxation time $1/\tau$ vs. $\rho_c - \rho_0$ for different wave-vectors in the cases of (a) 3-mers (B) and (b) angled objects (C). In the case of 3-mers (Fig. 9(a)), $\tau(q_n; \rho_0)$ displays a power law divergence at $\rho_c \lesssim 1$ only for the smallest wave vectors q_n. Increasing $q_n = (2\pi/L)n$, no divergence is observed at the ρ_c, signaling that no structural arrest occurs over length scales less than the box size L. Qualitatively similar results are obtained for the behavior of structural relaxation time τ in the case of the angled objects (C) (see Fig. 9(b)). However, for the angled objects (C) there is dynamical transition in this model, i.e. the structural arrest seems to happen at the critical density $\rho_c \approx 0.795$ which is lower than the jamming density $\rho_{jam} \approx 0.834$. In addition, we estimated the critical densities ρ_c for various objects. For objects (B), (C), (D), (F), (H), and (I) we obtained $\rho_c = 0.995 \pm 0.03$, 0.795 ± 0.04, 0.859 ± 0.04, 0.754 ± 0.04, 0.762 ± 0.04, and 0.661 ± 0.06, respectively.

Finally, we investigated the dependence of SISF, $F_s(q_n, t)$, on the rotation probability P_{rot}. Fig. 10 gives $\tau(q_n; \rho_0)$ vs. q_n for various P_{rot} in the case of angled objects (C) at density $\rho_0 = 0.80$. It is seen that relaxation time $\tau(q_n)$ decreases very rapidly with increasing rotation probability P_{rot}. Fickian behavior, $\tau \approx q_n^{-2} D_s^{-1}$, is obeyed for almost all q_n at high P_{rot}. When P_{rot} decreases, normal diffusive behavior is restricted to smaller and smaller q_n. Other objects yield similar behavior (see, e.g., Fig. 15 in Ref. [16]).
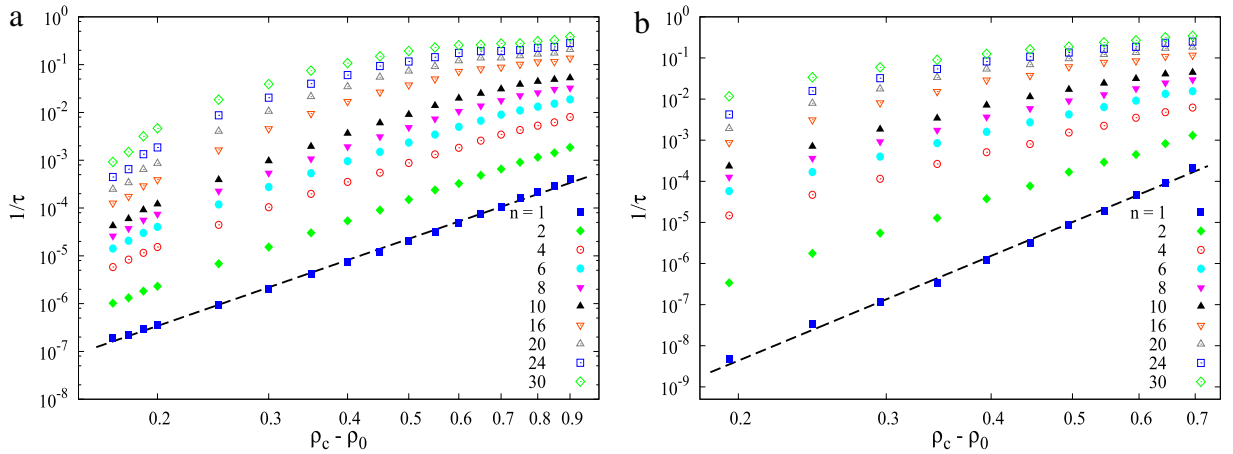
Fig. 9. (Color online) The inverse relaxation time, $1/\tau$, extracted from the SISF of (a) 3-mers (B) and (b) angled objects (C), as a function of $\rho_c - \rho_0$ ((a) $\rho_c = 0.995 \pm 0.03$, (b) $\rho_c = 0.795 \pm 0.04$). The symbols correspond to the wave vectors $\vec{q} = (q_n, 0)$, where $q_n = (2\pi/L)n$ and $n = 30, 24, 20, 16, 10, 8, 6, 4, 2, 1$ (from top to bottom). The dashed lines are the power-law fits of Eq. (8) for $q_n^{\min} = 2\pi/L$, where (a) $\varkappa = 4.58 \pm 0.14$, and (b) $\varkappa = 8.47 \pm 0.20$.
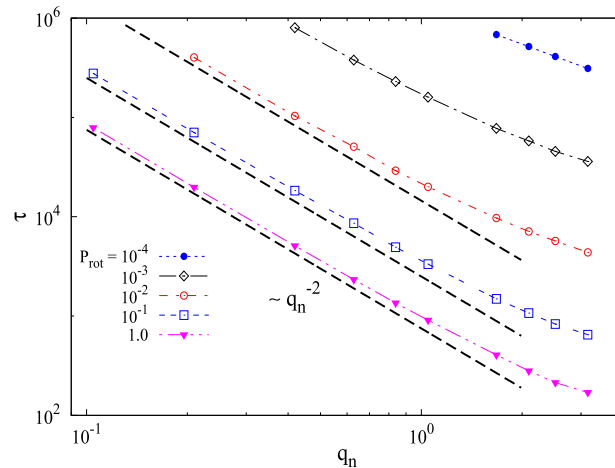

Fig. 10. (Color online) The relaxation time $\tau(q_n)$ for the case of object (C) at density $\rho_0 = 0.80$, as a function of the wave vector q_n. The symbols correspond to $P_{rot} = 10^{-4} - 1$ as indicated in the legend. The dashed black lines have slope -2 and are a guide for the eye.

4. Concluding remarks

In this paper we have consider a 2D lattice gas model, based on the concept of geometrical frustration which is generated by the particle shape. In order to examine influence of shape on the percolation and diffusion characteristics of the system, a systematic approach was made by examining a wide variety of object shapes. The shapes are made by self-avoiding lattice steps.

First, jamming coverage ρ_{jam} and percolation threshold ρ_p^* were determined for objects of various shapes and sizes. We have pointed out that for various objects of the same length, the percolation threshold of more compact shapes exceeds the percolation threshold of elongated ones.

The self-diffusion properties of the system have investigated through the mean-square displacement. We have found that, especially for large densities, the suppression of rotational motion leads to a pronounced cage effect. It can be observed as an intermediate region of anomalous diffusion in the mean-square displacement. Our results indicate that there is a significant difference in the diffusive behavior of the line segments and the other objects from Table 1. In the case of line segments, there is no critical density lower than the closest packing limit at which a structural arrest of the system occurs. However, particle mobility may be reduced if the object covers nodes outside its own axis. For such objects, the critical density ρ_c at which significant structural changes occur in the system is much smaller than the jamming density.

The most interesting results came from the analysis of the self-intermediate scattering function $F_s(\vec{q}, t)$. We have found that near the percolation threshold ρ_p^*, the decay of $F_s(\vec{q}, t)$ to zero occurs via the power-law for sufficiently low wave-vectors. At the lower densities of ρ_p^*, the long-time decay of $F_s(\vec{q}, t)$ is characterized by a stretched exponential behavior (7). If the density increases above ρ_p^*, the decay becomes slower and slower, showing a logarithmic-like behavior. Note that this

kind of decay with a stretched exponential and a power law resembles the relaxation behavior found in three-dimensional Ising spin glasses [51].

We have considered the behavior of the relaxation time τ as a function of the density ρ_0. We have shown that for the sufficiently small wave vectors (large length scales), relaxation times $\tau(q_n; \rho_0)$ display a power-law divergence (Eq. (8)) at densities around or below the closest packing limit ρ_{CPL}. In the case of line segments (k-mers), the critical density ρ_c cannot be distinguished from the $\rho_{CPL} \lesssim 1$. For the other objects, our results established the existence of a nontrivial divergence of $\tau(q_n; \rho_0)$ at a shape-dependent critical density ρ_c much above the percolation threshold ρ_p^* and below the jamming density ρ_{jam}. In the other words, there is dynamical transition in this model, i.e. critical density $\rho_c < \rho_{CPL}$ exists at which a structural arrest of the system takes place.

By introducing a rotation of objects we have analyzed the interplay between the kinetic constraints and diffusional dynamics in the model. We have shown that for all objects, the relaxation times decrease very rapidly with increasing rotation probability P_{rot}. The slowdown of the system that becomes more significant as P_{rot} is decreased can be attributed to the fact that the dynamics of an object moving on a lattice is dictated by geometric exclusion effects.

Acknowledgments

References

[1] R. Metzler, J. Klafter, J. Phys. A: Math. Gen. 37 (2004) R161.
[2] P.J. Lu, E. Zaccarelli, F. Ciulla, A.B. Schofield, F. Sciortino, D.A. Weitz, Nature 453 (2008) 499.
[3] G. Drazer, D.H. Zanette, Phys. Rev. E 60 (1999) 5858. http://dx.doi.org/10.1103/PhysRevE.60.5858.
[4] J. Kurzidim, D. Coslovich, G. Kahl, Phys. Rev. Lett. 103 (2009) 138303. http://dx.doi.org/10.1103/PhysRevLett.103.138303.
[5] P. Gallo, M. Rovere, J. Phys.: Condens. Matter 15 (2003) 7625.
[6] P. Gallo, M. Rovere, S.-H. Chen, J. Phys.: Condens. Matter 22 (2010) 284102.
[7] E.R. Weeks, D.A. Weitz, Chem. Phys. 284 (2002) 361.
[8] R. Hilfer, Chem. Phys. 284 (2002) 399.
[9] G. Marty, O. Dauchot, Phys. Rev. Lett. 94 (2005) 015701.
[10] A. Fiege, T. Aspelmeier, A. Zippelius, Phys. Rev. Lett. 102 (2009) 098001. http://dx.doi.org/10.1103/PhysRevLett.102.098001.
[11] M. Weiss, H. Hashimoto, T. Nilsson, Biophys. J. 84 (2003) 4043.
[12] K. Ritchie, X.-Y. Shan, J. Kondo, K. Iwasawa, T. Fujiwara, A. Kusumi, Biophys. J. 88 (2005) 2266.
[13] M.D. Ediger, Annu. Rev. Phys. Chem. 52 (2000) 99.
[14] P. Chaudhuri, L. Berthier, W. Kob, Phys. Rev. Lett. 99 (2007) 060604.
[15] A. Patti, D. El Masri, R. van Roij, M. Dijkstra, Phys. Rev. Lett. 103 (2009) 248304. http://dx.doi.org/10.1103/PhysRevLett.103.248304.
[16] J.R. Šćepanović, I. Lončarević, L. Budinski-Petković, Z.M. Jakšić, S.B. Vrhovac, Phys. Rev. E 84 (2011) 031109. http://dx.doi.org/10.1103/PhysRevE.84.031109.
[17] J. Kärger, D.M. Ruthven, Diffusion in Zeolites and Other Microporous Solids, Wiley, New York, 1992.
[18] C. Baerlocher, W.M. Meier, D.H. Olson, Atlas of Zeolite Structure Types, Elsevier, London, 2001.
[19] A. Brzank, G.M. Schütz, P. Bräuer, J. Kärger, Phys. Rev. E 69 (2004) 031102. http://dx.doi.org/10.1103/PhysRevE.69.031102.
[20] Lj. Budinski-Petković, U. Kozmidis-Luburić, Phys. Rev. E 56 (1997) 6904.
[21] J.W. Evans, Rev. Modern Phys. 65 (1993) 1281.
[22] V. Privman, Colloids Surf. A 165 (2000) 231.
[23] A. Cadilhe, N.A.M. Araújo, V. Privman, J. Phys.: Condens. Matter 19 (2007) 065124.
[24] I. Lončarević, Z.M. Jakšić, S.B. Vrhovac, Lj. Budinski-Petković, Eur.Phys. J. B 73 (2010) 439.
[25] M.E.J. Newman, R.M. Ziff, Phys. Rev. E 64 (2001) 016706. http://dx.doi.org/10.1103/PhysRevE.64.016706.
[26] I. Lončarević, Lj. Budinski-Petković, S.B. Vrhovac, Eur. Phys. J. E 24 (2007) 19.
[27] Lj. Budinski-Petković, S.B. Vrhovac, I. Lončarević, Phys. Rev. E 78 (2008) 061603.
[28] D. Staufer, A. Aharony, Introduction to Percolation Theory, Taylor & Francis, London, 1994.
[29] R. Metzler, J. Klafter, Phys. Rep. 339 (2000) 1.
[30] V. Privman, P. Nielaba, Europhys. Lett. 18 (1992) 673.
[31] J.W. Lee, B.H. Hong, J. Chem. Phys. 119 (2003) 533.
[32] I. Lončarević, Lj. Budinski-Petković, S.B. Vrhovac, A. Belić, Phys. Rev. E 80 (2009) 021115.
[33] J. Colmenero, F. Alvarez, A. Arbe, Phys. Rev. E 65 (2002) 041804. http://dx.doi.org/10.1103/PhysRevE.65.041804.
[34] W. Kob, H.C. Andersen, Phys. Rev. E 51 (1995) 4626. http://dx.doi.org/10.1103/PhysRevE.51.4626.
[35] S. Mossa, R. Di Leonardo, G. Ruocco, M. Sampoli, Phys. Rev. E 62 (2000) 612. http://dx.doi.org/10.1103/PhysRevE.62.612.
[36] W. van Megen, J. Phys.: Condens. Matter 14 (2002) 7699.
[37] P.M. Reis, R.A. Ingale, M.D. Shattuck, Phys. Rev. Lett. 98 (2007) 188301.
[38] R. Candelier, O. Dauchot, G. Biroli, Phys. Rev. Lett. 102 (2009) 088001.
[39] W. Kob, H.C. Andersen, Phys. Rev. E 48 (1993) 4364.
[40] J. Jäckle, A. Krönig, J. Phys.: Condens. Matter 6 (1994) 7633.
[41] A.C. Pan, J.P. Garrahan, D. Chandler, Phys. Rev. E 72 (2005) 041106. http://dx.doi.org/10.1103/PhysRevE.72.041106.
[42] L. Berthier, D. Chandler, J.P. Garrahan, Europhys. Lett. 69 (2005) 320.
[43] O. Dauchot, G. Marty, G. Biroli, Phys. Rev. Lett. 95 (2005) 265701.
[44] A. Fierro, T. Abete, A. Coniglio, J. Chem. Phys. 131 (2009) 194906.
[45] E. Del Gado, A. Fierro, L. de Arcangelis, A. Coniglio, Europhys. Lett. 63 (2003) 1.
[46] E.D. Gado, A. Fierro, L.d. Arcangelis, A. Coniglio, Phys. Rev. E 69 (2004) 051103. http://dx.doi.org/10.1103/PhysRevE.69.051103.
[47] T. Abete, A. de Candia, E.D. Gado, A. Fierro, A. Coniglio, Phys. Rev. Lett. 98 (2007) 088301. http://dx.doi.org/10.1103/PhysRevLett.98.088301.
[48] T. Abete, A. de Candia, E. Del Gado, A. Fierro, A. Coniglio, Phys. Rev. E 78 (2008) 041404.
[49] C. Fusco, P. Gallo, A. Petri, M. Rovere, Phys. Rev. E 65 (2002) 026127.
[50] A. Díaz-Sánchez, A. de Candia, A. Coniglio, J. Phys. A: Math. Gen. 35 (2002) 3359.
[51] A.T. Ogielski, Phys. Rev. B 32 (1985) 7384. http://dx.doi.org/10.1103/PhysRevB.32.7384.